Journal of Materials Science: Materials in Electronics (2018) 29:15621–15631
https://doi.org/10.1007/s10854-018-9154-5

Characterization of structural and optical properties of the mesoporous Ce-MCM-41 hybrid materials

O. A. González Vargas[1] · J. A. De los Reyes Heredia[2] · V. A. Suárez-Toriello[3] · R. Hurtado Rangel[1] · J. A. Wang[4] · L. F. Chen[4]

Received: 9 November 2017 / Accepted: 20 April 2018 / Published online: 27 April 2018

Abstract
Ce-modified mesostructured MCM-41-type hybrid materials with different Si/Ce molar ratios (Si/Ce = 10, 30 and 50) were synthesized by the surfactant-assisted hydrothermal method and their structural and optical properties were characterized by small angle X-ray scattering (SAXS), field emission scanning electron microscopy (FE-SEM) equipped with embedded EDS system, ultraviolet and visible diffuse reflectance (UV–vis DR) spectroscopy, X-ray photoelectron spectroscopy (XPS) and Raman spectroscopy. Ce-MCM-41 samples show highly ordered 2D porous hexagonal mesostructures and oval and spherical morphologies with particle size between 300 and 600 nm, depending on the incorporated Ce amount. Incorporation of Ce^{4+} into ordered mesoporous silica generates oxygen defects in ceria-silica composites with the formation of Ce^{3+} species as confirmed by the XPS analyses. Cerium incorporation modified their structural regularity and resulted in an effective red shifting of the band gap (2.82 eV at 2.64 eV) due to the creation of intermediate energy states. Both asymmetry and broadening of Raman active F_{2g} mode confirmed the presence of the structural defects. These ordered mesoporous Ce-MCM-41 hybrid materials are potentially attractive for their use as novel photocatalysts in the degradation of organic pollutants present in wastewater employing UV and visible light.

1 Introduction

Porous solid materials such as zeolites, MCM-41, MCM-48 and SBA-15 are frequently used as catalytic supports for immobilizing and dispersing the active phases thereby increasing the number of active sites in the final catalyst. Different transition metal elements (e.g. Ti, Cr, Fe, V, etc.) can be implanted and distributed into the silica matrix [1, 2], inducing several modifications in both the acid-base properties and the UV absorption spectrum of the corresponding semiconductor. Moreover, many adsorbents provide rich hydroxyl groups in surface which favor the photocatalytic processes [3]. In this way, the so-called Adsorbent-Photocatalysts Hybrids (APHs) are bifunctional solids with adsorption and photocatalytic properties; they are a very promising kind of functional materials [4]. The synergy created from these two capacities leads to composites endowing with superior catalytic activity and higher selectivity toward the desired reaction products precisely for the transfer of species from the adsorbent sites to the semiconductor ones and vice versa. The enhanced properties of APHs have been applied in different photocatalytic applications that include hydrogen production, CO_2 photoreduction, organic synthesis, abatement of organic pollutants in wastewater and gas phase, and indoor air treatment [5].

Both adsorption ability and shape selectivity of ordered mesoporous MCM-41 silica make it an excellent candidate to prepare APH composites. It is reported that CeO_2 is a very important semiconductor or photocatalyst that has recently

✉ O. A. González Vargas
ogonzalezv@ipn.mx

[1] Departamento de Ingeniería en Control y Automatización, Escuela Superior de Ingeniería Mecánica y Eléctrica–Zacatenco, Instituto Politécnico Nacional, UPALM, Col. Lindavista, Del. Gustavo A. Madero, 07738 Mexico City, Mexico

[2] Departamento de Ingeniería de Procesos e Hidráulica, Universidad Autónoma Metropolitana–Iztapalapa, Av. San Rafael Atlixco No. 186, Col. Vicentina, Del. Iztapalapa, 09340 Mexico City, Mexico

[3] CONACyT-CIATEC A.C. Centro de Innovación Aplicada en Tecnologías Competitivas, Omega No. 201, Col. Industrial Delta, 37545 León, Gto., Mexico

[4] Escuela Superior de Ingeniería Química e Industrias Extractivas, Instituto Politécnico Nacional, Av. Politécnico s/n, Col. Zacatenco, 07738 Mexico City, Mexico

been utilized in several photocatalysis processes [6–9]. However, its photocatalytic activity is still not considerable for practical applications with solar light due to the low light absorption efficiency (E_g = 3.2 eV) and the high recombination rate of photogenerated electron–hole pairs [10]. In this sense, the incorporation of CeO_2 into the mesopores or structure of MCM-41 molecular sieve constitutes an interesting strategy to improve its photocatalytic performance. Under UV and/or visible light irradiation, these Ce-MCM-41-type hybrid materials may be promising systems for environmental and energy applications.

In this paper, based on the pure CeO_2, we photoelectrically evaluated the synergic effect of Ce-doped MCM-41 structure that can extend the light absorption range to the visible region and produce highly energetic electron–hole pairs. Particularly, oxygen vacancies (V_O) and Ce^{3+} species present in ceria nanostructures result in a red shifting for its band gap [11, 12]. We have attempted to investigate how different Ce contents incorporation into mesostructured MCM-41 silica can induce defects sites formation and narrows the band gap of CeO_2 by changing its structural regularity. Formations of Ce^{3+} species and oxygen defects were well characterized by X-ray photoelectron and Raman spectroscopic techniques, respectively. Qualitative analysis of the effect of Ce-loading into the silicate network of the mesoporous Ce-MCM-41 hybrid materials on their structural, optical and chemical properties was reported.

2 Experimental section

2.1 Synthesis of Ce-MCM-41 hybrid materials

The details of experimental procedure used to prepare the ordered mesoporous MCM-41-type ceria-silica composites were previously reported in our research article [13]. The surfactant-assisted hydrothermal method in static conditions was used to obtain Ce-MCM-41 hybrid materials with different Si/Ce molar ratios (50, 30 and 10). Tetraethyl orto-silicate (TEOS, stream chemicals) and hexahydrate cerium nitrate ($Ce(NO_3)_3{\cdot}6H_2O$, 99%, Aldrich) were used as silicon and cerium precursors, respectively. Cethyltrimethylamonium bromide in powder (CTAB, 99% pure, Sigma) was employed as structure-directing agent. Ammonium hydroxide (NH_4OH at 27%, J.T. Backer) was used as precipitating chemical in the basic synthesis media. In a typical synthesis, 2.28 g CTAB was dissolved in 100 ml of deionized H_2O. Under continuous stirring, the proper amount (8.5 ml) of NH_4OH was slowly added to the principal solution and then 5.7 ml of TEOS (pH 11.0–11.3) were added dropwise into above mixture. Subsequently, just as quickly, a calculated $Ce(NO_3)_3$ solution (0.05 M) was added in order to obtain a specified Si/Ce molar ratio in the final product. The final blend was stirred for one additional hour. Then, the synthesis gel was poured into a Teflon bottle and was tightly sealed. The reaction was performed in a vacuum oven (Lab-Line Instruments, Inc., model 3608, power 600 W) at 95 °C for 96 h under static conditions. After cooling to room temperature, the resultant precipitate was recovered by filtration and washed with deionized H_2O several times to remove any possible ionic or organic remnants. At last, the product was dried using an air flow within an exhaust hood overnight. The dried mesoporous ceria-silica composite (denominate as Ce-MCM-41-50) was calcined in static air in two stages. In the first stage, the solid was treated at 350 °C for 4 h employing a heating ramp of 3 °C/min. Then a heating rate of 2 °C/min was programmed to increase the temperature up 600 °C where the sample was remained for 4 h. A similar procedure was carried out for the synthesis of the others Ce-MCM-41 hybrid materials with Si/Ce molar ratio of 30 and 10.

As reference materials, pure CeO_2 and MCM-41 silica powders also were prepared. The synthesis of CeO_2 with high specific area was carried out from the incorporation of the molecules of the template (CTAB) in the hydrated CeO_2 in order to provide an ordered pore structure. At the beginning of the preparation, the NH_4OH was slowly added to a vigorously stirred aqueous solution of CTAB surfactant (0.0625 M). Subsequently, a 0.125 M aqueous solution of $Ce(NO_3)_3$ was added dropwise. Then, the precipitation of the hydrated CeO_2 with the appearance of a slightly brown gelatinous solid was observed. The resulting mixture was deposited in a thermostatic bottle and maintained at 95 °C for 96 h. Finally, the formed solid was filtered and washed with deionized water. The yellow powder was dried in an extraction hood for 2 days and subsequently calcined at 500 °C.

2.2 Characterization of Ce-MCM-41-type photocatalysts

Nitrogen adsorption–desorption isotherms of synthesized Ce-MCM-41-type ceria-silica composites were obtained on a Quantachrome Autosorb 1 apparatus using a static adsorption procedure at − 195 °C. Prior to the adsorption measurements, all samples were degassed at 120 °C in vacuum for 4 h. Then, the isotherms were measured over a relative pressure range from $P/P_0 = 1 \times 10^{-6}$ to 0.995. The specific area was calculated applying the BET method using adsorption data in a P/P_0 range between 0.05 and 0.30. The pore size distributions were calculated from desorption branch data of each isotherm using the BJH method, which is suitable for pores with limited ordered domains (singly resolved peaks in SAXS) despite the polydispersity in their diameters [14, 15]. The cumulative pore volume was obtained from the isotherms at $P/P_0 = 0.995$.

The small angle X-ray scattering (SAXS) experiments were realized at ambient temperature employing a Kratky camera coupled a cupper anode tube whose monochromatic CuK_α radiation was selected with a Ni filter. The distance between the sample and the proportional linear counter was of 25 cm. Before data recording, each sample was introduced inside a capillary tube and the dispersion intensity was measured for 9 min to obtain statistical significance. The SAXS curves were obtained varying the angle of the distance between the sample and the detector in the 8.53×10^{-4} Å^{-1} < s < 0.47 Å^{-1} interval. The scattering vector is defined as $s = (2/\lambda) \times (\sin\theta)$, where λ is the wavelength (1.5418 Å) and 2θ is the scattering angle. From the angular parameter (q) defined as $q = (4\pi/\lambda) \times (\sin\theta) = 2\pi s$, it is possible to estimate the Bragg-spacing using the relation $d_{100} = 2\pi/q^* = 1/s^*$, where q^* and s^* are the respective values for the maximum (100) peak [16].

Direct images at nanometric level to estimate the morphology and the particle size of the Ce-MCM-41 hybrid materials were obtained with a field emission scanning electron microscope (FE-SEM, JEOL JSM-7800F) equipped with a backscattered electron detector, which is sensitive to the atomic number variation of the present elements in the samples. The microscope was operated with an acceleration voltage of 5–10 kV.

UV–vis diffuse reflectance spectra (UV–vis DRS) of Ce-MCM-41 samples and reference CeO_2 were obtained on a Varian Cary 5E spectrophotometer equipped with an integration sphere attachment on the wavelength range of 200 nm at 800 nm. All spectra in absorbance mode were recorded at ambient conditions using MgO as certificated reference. Band gap (Eg) energies of all samples were determined conforming to the analytical method reported by Katta et al. [17] employing the equation $Eg(eV) = 1239.8/\lambda_{AE}$ (nm), where λ_{AE} is the wavelength corresponding to the absorption edge in each spectrum.

X-ray photoelectron spectroscopy (XPS) spectra of the solids were collected using a K-alpha Thermo Scientific spectrometer with a monochromatic AlK_α (1486 eV) radiation source and a hemispherical electron analyzer having an energy resolution of 0.5 eV. The measurements were done at room temperature and samples were maintained in vacuum (below 4×10^{-10} Torr) into the spectrometer chamber during the analyses. Binding energies measured have an uncertainty of ± 0.2 eV. All XPS spectra were corrected by setting the binding energy of the adventitious carbon (C 1s) peak at 284.6 eV. The XPS spectra analysis was performed using Thermo Scientific Avantage software.

Raman spectra of the samples were recorded with LabRam HR800 Horiba-Jobin Yvon high resolution Raman spectrometer fitted with a confocal microscope. Samples were excited either using 532 nm Ar ion laser which was focused on the sample under the microscope with the diameter of the analyzed spot being ~ 1 µm. All Raman spectra were obtained in the 1500–100 cm^{-1} range with a spectral resolution of 0.5 cm^{-1}. For each spectrum the buildup time was of 10 scans. For data acquisition, the LabSpec 5 software was employed.

3 Results and discussion

3.1 Textural properties—N_2 physisorption analysis

The textural properties of the ordered mesoporous Ce-MCM-41 hybrid materials were measured by N_2 physisorption isotherm method. The textural data are reported in Table 1. According to N_2 physisorption analysis, a decrease

Table 1 Nominal content of Ce, physicochemical properties and concentration of silanol groups for the mesoporous ceria-silica composites

Material[a]	Ce (wt%)	S_{BET}[b] (m^2/g)	V_t[c] (cm^3/g)	D_{BJH}[d] (nm)	d_{100}[e] (nm)	a[f] (nm)	w[g] (nm)	[SiOH][h] (mmol/g)
MCM-41	0.0	1129	0.6	2.44	4.25	4.91	2.47	14.4
Ce-MCM-41-50	2.9	884	0.9	2.43	4.38	5.07	2.63	14.4
Ce-MCM-41-30	4.8	891	1.3	2.45	4.35	5.03	2.58	14.5
Ce-MCM-41-10	13.2	684	1.4	2.17	3.89	4.50	2.33	14.1

[a]Final number denote the TEOS/cerium nitrate molar ratio used in synthesis gel

[b]BET specific area

[c]Pore total volume at $P/P_0 = 0.99$

[d]Mean pore diameter obtained by BJH method [13]

[e]Bragg spacing ($d_{100} = 2\pi/q^* = 1/s^*$, where q^* and s^* are the respective values for the maximum (100) peak) for hexagonal *p6mm* mesoporous structure [16]

[f]Unit cell parameter ($a = 2d_{100}/\sqrt{3}$) for hexagonal *p6mm* mesostructure [13]

[g]Pore wall thickness ($w = a - D_{BJH}$) for hexagonal *p6mm* mesostructure [13]

[h]Obtained from the Q_2, Q_3, and Q_4 data of ^{29}Si MAS NMR analysis included in reference [13] and the procedure exposed by Wouters et al. [35]

of both specific area and pore diameter was observed while pore volume increases as Ce-content into the silicate network increased. For example, specific area, pore diameter and pore volume were measured to be 884 m^2/g, 24.3 Å and 0.9 cm^3/g for Ce-MCM-41-50 (2.9 wt% Ce) material, whereas 684 m^2/g, 21.7 Å and 1.4 cm^3/g were found for Ce-MCM-41-10 (13.2 wt% Ce) material [13]. The MCM-41 structure with a well-ordered hexagonal pores array was preserved after the Ce incorporation and thermal treatments.

3.2 Structural features—SAXS analysis

The SAXS analysis is a feasible technique to the structural characterization of mesoporous materials. Figure 1 shows that all SAXS patterns of the silica/ceria-silica materials exhibited an intense peak for the scattering vector (s), in the range of 0.023–0.026 $Å^{-1}$, which is assigned to the (100) reflection of the hexagonal porous framework. No other peaks were observed, indicating that only a modest mesoscopic ordering was formed in these materials. These results show that the Ce-MCM-41-type solids have a 2D porous hexagonal (*p6mm*) mesostructure [18]. Nevertheless, a slight widening for the (100) reflection can be observed for the Ce-modified MCM-41 silica, representing a decrease of long-range ordering, as result of an increment in the Ce content into framework (Fig. 1c-d). These results strongly confirm formation of Ce–O–Si bonds in the silicate network. In addition, at wide angle ($2\theta > 10°$) no additional diffraction peaks were observed, indicating an aperiodic nature of these Ce-modified silicate inorganic frameworks [19]. This also implies a homogeneous dispersion of ceria into the structure of Ce-MCM-41 samples.

Figure 1b shows the SAXS pattern of the calcined mesoporous ceria-silica material with Si/Ce molar ratio equal to 50, indicating that this silica sample with a low amount of incorporated Ce (2.9 wt%) is regularly ordered with a 2D hexagonal (*p6mm*) mesostructure. On the contrary, curve (d) in Fig. 1 refers to Ce-doped silica particles prepared via the hydrothermal method using the TEOS/$Ce(NO_3)_3{\cdot}6H_2O$ molar ratio = 10 and shows a slight displacement of the (100) peak assigned to the hexagonal lattice structure. Therefore, the incorporation of a greater amount of Ce (13.2 wt%) into the MCM-41 structure can produce sites with defects and tense bonds that lead to a partial collapse of the pore system and a decrease in the structural regularity. Thus, the Bragg spacing or interplanar distance (d_{100}) values obtained from the Bragg peak indexed as (100) slightly decreased but remained in the range of 4.38–3.89 nm for all three mesostructured Ce-MCM-41 materials (see Table 1). The values of lattice cell parameters (a) determined from the individual values of d_{100}-spacing by the equation $a = 2d_{100}/\sqrt{3}$ were between 5.07 and 4.50 nm. The wall thickness (w) calculated with the corresponding cell parameters (a) and pore diameters (D_{BJH}) varied in the range of 2.6–2.3 nm. Sayari et al. [14] suggested that both a high specific area and a large pore volume would contribute to extremely thin pore walls, which in turn, result in materials with low stability. We observed the conservation of the ordered mesostructure after incorporation of a high Ce loading (13.2 wt%) into silicate network. This result was similar to the report of mesoporous hexagonal (*p6mm*) ceria-silica with high Ce loading employing $Ce(OH)_4$ as Ce precursor [20]. Therefore, it is possible that mesoporous Ce-MCM-41-type ceria-silica composites can be prepared using $Ce(NO_3)_3{\cdot}6H_2O$ and TEOS under basic conditions.

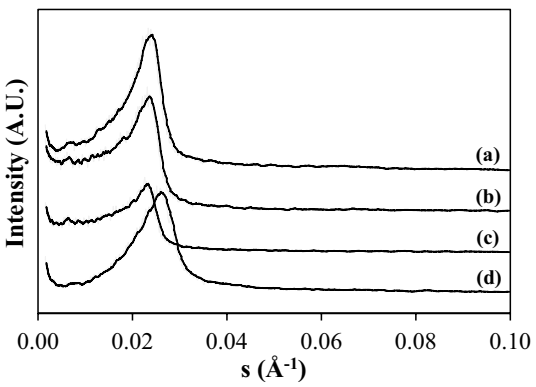

Fig. 1 SAXS patterns for mesoporous Ce-MCM-41-type ceria-silica composites. (*a*) MCM-41, (*b*) Ce-MCM-41-50, (*c*) Ce-MCM-41-30, (*d*) Ce-MCM-41-10

3.3 Morphological feature: FE-SEM analysis

FE-SEM images were obtained to investigate the morphology and diameter of Ce-MCM-41 particles. Figure 2a shows the SEM image of the Ce-MCM-41-50 sample where ceria-silica nanoparticles of regular geometrical shape (oval and spherical) with a particle size greater than 600 nm were observed. The other ceria-silica samples with Si/Ce molar ratio equal to 30 and 10 also showed a similar morphology although the particle sizes decreased as the Ce content increased. The SEM micrographs of the Ce-MCM-41-30 and Ce-MCM-41-10 materials (Fig. 2b, c) exhibit a particle diameter around 500 and 300 nm, respectively, similar to the sizes obtained in another synthesis for different research groups. For example, Cho et al. [21] reported a particle size of ~ 500 nm to mesoporous Ce-MCM-41-type silica with a Si/Ce molar ratio equal to 5. With the help of backscattered electron detector, a considerable amount of Ce-based nanometric particles dispersed on the surface of interconnected ceria-silica particles was observed (Fig. 2b, c). For a better appreciation, Fig. 2d shows the SEM image in high resolution taken with the secondary electron detector from the sample with high Ce loading (Ce-MCM-41-10).

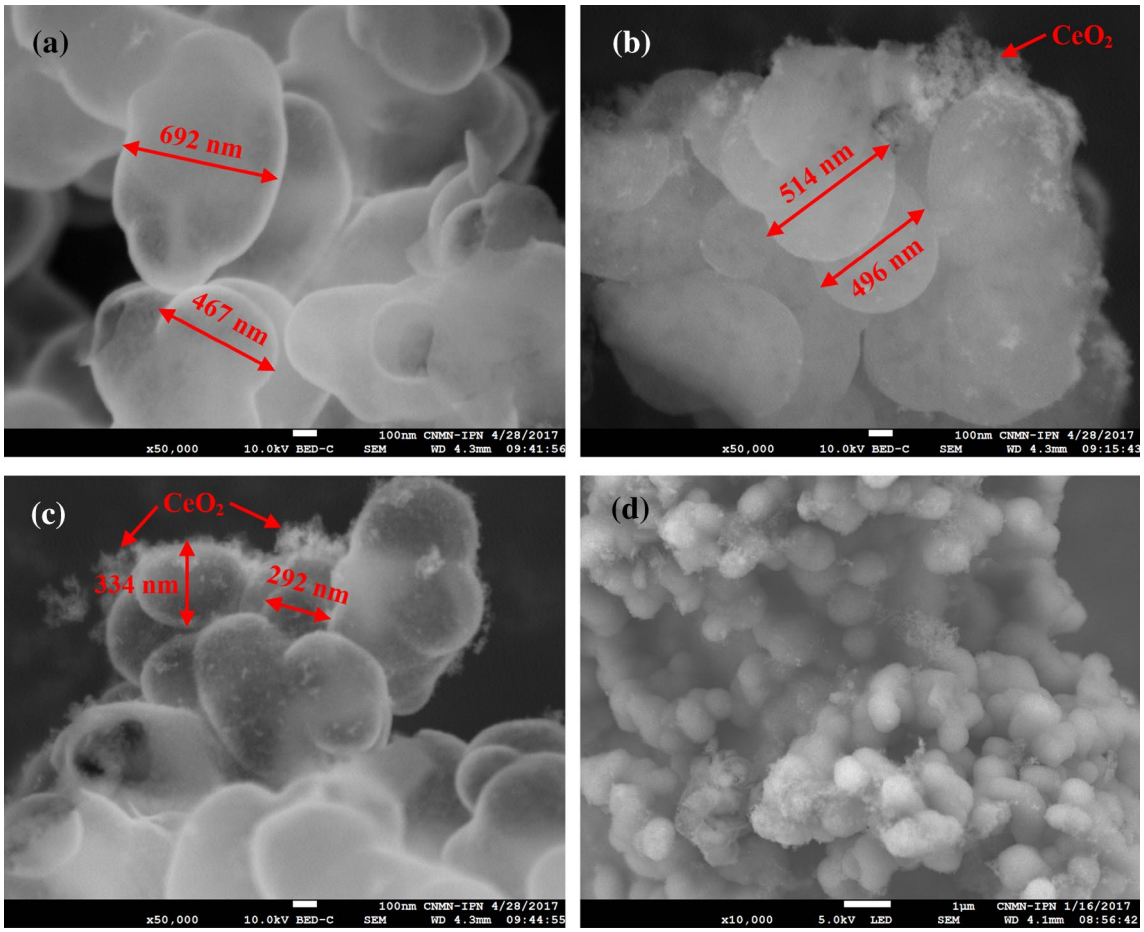

Fig. 2 FE-SEM images of mesoporous ceria-silica composites. (**a**) Ce-MCM-41-50, (**b**) Ce-MCM-41-30, (**c**) and (**d**) Ce-MCM-41-10

In this micrograph, some Ce ions were not incorporated in the Si–O–Si network but are present as nanometric clusters of CeO_2 segregated to the surface. As can be seen in the Fig. 2b, c, the particle size of the ceria segregated on surface of Ce-MCM-41-30 and Ce-MCM-41-10 samples is approximately of 5 nm. However, for the hybrid material with the highest Ce loading (13.2 wt%), ceria nano-clusters on its surface were identified by a XRD analysis (not shown) with weak diffraction peaks at $2\theta = 28.6°$, 47.6° and 56.1°, which are referred to (111), (220) and (311) reflection planes of cubic CeO_2 (JCPDS 034-0394), respectively.

Elemental mapping images for Si, O and Ce species were also recorded using the FE-SEM technique with an embedded system of energy dispersive X-ray spectroscopy (EDS). The SEM–EDS images from the representative Ce-MCM-41-30 sample are shown in Fig. 3. The image in low amplification of the Fig. 3a shows that the shapes of the particles are mostly spherical and oval. In addition, from the qualitative analysis data obtained from the studied surface, the spatial distributions of Si (Fig. 3b) and O (Fig. 3c) species are highly homogeneous in all analysis area. However, in comparison to these elements, Ce species are localized only in specific small zones where it was segregated (Fig. 3d). The obtained results from EDS analysis for the corresponding mapping images provided a Ce content of 4.31, 5.67 and 14.7 wt% to samples with Si/Ce molar ratio equal to 50, 30 and 10, respectively, which are similar to nominal Ce-loading (Table 1).

3.4 Optical properties—UV–vis DR spectroscopy

UV–vis DRS measurement is a reliable method to obtain information about charge transfer bands between the metal ion and oxygen. The UV–vis DRS of pure CeO_2 and mesoporous ceria-silica composites calcined at 600 °C are shown in Fig. 4. As can be seen in Fig. 4a, the crystalline CeO_2 strongly absorb light in the UV region and presented two wide bands around 256 and 367 nm which correspond to the charge transfer from O^{2-} to Ce^{4+}, specifically, the O $2p^6 \rightarrow$ Ce $4f^0$ electronic transition [22]. In particular, the band centered at 256 nm is related to the Ce^{4+} ion present in tetrahedral coordination (Ce^{4+}_{Th}); while the absorption band

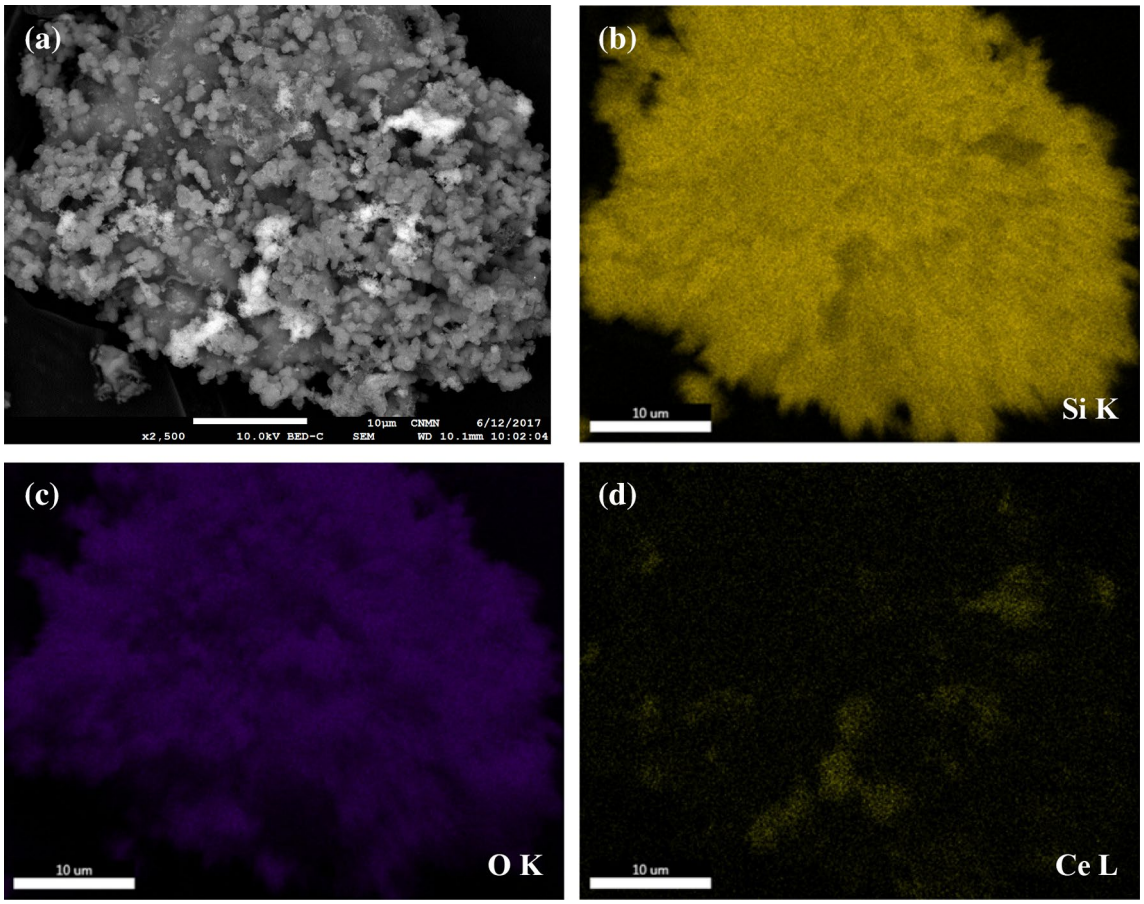

Fig. 3 SEM-EDS images of mesoporous Ce-MCM-41-30 ceria-silica composite

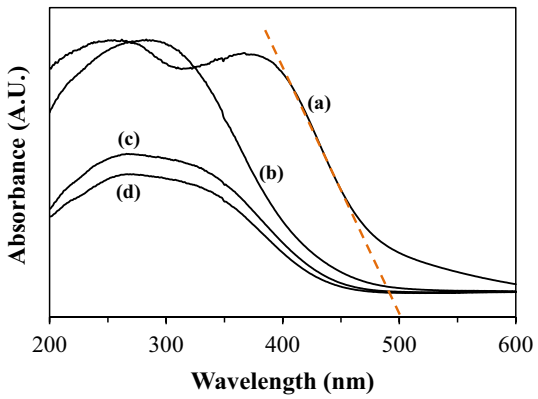

Fig. 4 UV–vis DRS of the Ce-doped mesostructured silica composites. (*a*) CeO_2, (*b*) Ce-MCM-41-10, (*c*) Ce-MCM-41-30 and (*d*) Ce-MCM-41-50

at lower energy (367 nm) corresponds to Ce^{4+} with octahedral coordination (Ce^{4+}_{Oh}) [23]. In the semiconducting CeO_2 material, the valence and conduction bands consist of O 2p and Ce 5d levels with a gap energy around 4 eV. Ce 4f level is present between these two states and just above Fermi level [24]. The band gap energy of all samples was estimated from the wavelength of adsorption edge (λ_{AE}) present in each UV–vis DR spectrum of the Fig. 4 through the procedure described in the experimental section. The beginning of light absorption to our reference CeO_2 (80 m^2/g) with a crystallite mean size of 12.5 nm was presented around 500 nm, according to extrapolating the slope of the linear part of the UV–vis DR spectrum (see Fig. 4a) until its intersection with the abscissas axis (wavelength). This gives rise to a band gap energy of 2.48 eV which is consistent with the characteristic values reported in the literature for different CeO_2 materials, taking into account the discrepancy that exist to interpret the bandwidths and the specular reflectance in the UV–vis DRS. For example, Ji et al. [25] for mesoporous CeO_2 (145 m^2/g) with a crystal size of 5.1 nm showed a UV–vis DR spectrum where the light absorption beginning was localized at 420 nm with a band gap value of 2.95 eV. Renuka et al. [26] presented the UV–vis DR spectrum for CeO_2 microplates (57 m^2/g) with nanocrystals of 4.1 nm which displayed a λ_{AE} value near 430 nm and the band gap estimated (E_g) was of 2.88 eV.

UV–vis DRS of the Ce-MCM-41 hybrid materials with different Si/Ce molar ratio are shown in Fig. 4b–d. These spectra show only one wide band of light absorption centered at approximately 266, 269 and 290 nm in the UV region when the Si/Ce molar ratio varied from 50 to 30 and 10, respectively. Similar to pure ceria, these contributions should be related to electron excitation from the O 2p band to the Ce 4f orbitals of Ce^{4+}. For all the mesostructured ceria-silica composites a similar procedure applied to reference CeO_2 was used to estimate their band gap values. In this way, the absorption edges presented a displacement to shorter wavelength region as the Si/Ce molar ratio decreased. For example, the λ_{AE} values of the samples were shifted from 470 to 465 nm and 440 nm, and the corresponding band gap energy increased from 2.64 to 2.67 eV and 2.82 eV as the Si/Ce molar ratio decreased from 50 to 30 and 10, respectively. Thus, there is an evident red shifting in the band gap for the Ce-MCM-41-50 (2.9 wt%) and Ce-MCM-41-30 (4.8 wt%) hybrid materials, compared to that Ce-MCM-41-10 sample with greater abundance of cerium (13.2 wt%). For the pure CeO_2, it has been established that a decrease in the particle size by a quantum confinement effect causes a displacement of the absorption band toward the higher energy zone (small wavelength) accompanied by an increment in the effective width of band gap (blue shift) [27]. In contrast, Patsalas et al. [28] have found that the red shift in the band gap is due to the presence of Ce^{3+} ions at grain boundaries and the E_g value decreases with the increase in Ce^{3+} concentration [Ce^{3+}] which forms some localized gap states in the band gap. Similarly, Tatar et al. [29] reported that the red shifting of band gap is due to formation of some localized band gap states which are caused by oxygen vacancies and Ce^{3+} ions.

The band gap energy of the studied materials is red shifted in the following order: CeO_2 (2.48 eV) < Ce-MCM-41-50 (2.64 eV) < Ce-MCM-41-30 (2.67 eV) < Ce-MCM-41-10 (2.82 eV). As aforementioned, the pure CeO_2 material has three valence/conduction bands that are mainly composed of the O 2p, Ce 5d and Ce 4f levels. The CeO_2-based materials frequently used in photocatalysis reactions have a band gap around 2.8 eV which originates from the O 2p to Ce 4f and Ce 5d electronic transitions requiring visible light excitation [6, 8–10]. Thus, when the 4f orbitals are unoccupied (Ce^{4+} f^0), the CeO_2 is considered as an insulating material with an energy gap between O 2p valence band and Ce 5d conduction band up to ~ 6.0 eV [30, 31]. Nevertheless, as discussed later in the sections of XPS and Raman analysis, the presence of Ce^{3+} ions in our reference CeO_2 material leads to an occupation of the 4f orbitals ($4f^1$), and hence, a charge transfer between Ce^{3+} and the conduction band ($4f^1 \rightarrow 5d$) and/or valence band ($2p \rightarrow 4f^1$) of CeO_2 results in a red shift of its band gap. In this case, an additional energy state can be created via the electrons transition from 4f to 5d orbitals allowing a greater light absorption at ~ 500 nm together with a characteristic band gap of ~ 2.5 eV converting the CeO_2 in a superior semiconductor photocatalyst [10, 32].

According to the physical properties of solid state, the band gap of a semiconductor material is the distance between the valence band which is full of electrons, and the conduction band which is completely empty. Therefore, the narrower this band distance, the easier for the electrons to move from one band to the other is. From the UV–vis DR spectral response of Fig. 4b–d, it became clear that the ability to absorb visible light of the mesoporous Ce-MCM-41 hybrid materials was improved when the Ce content was decreased in the silicate network. This phenomenon can be attributed to the presence of high concentration of Ce^{3+} species and oxygen vacancies (V_O), as evidenced by the XPS and Raman analysis. For example, for Ce-MCM-41-50 hybrid material, the single $4f^1$ electron in Ce^{3+} suffers $4f^1 \rightarrow 5d$ charge transfer transition and allows adsorption at 470 nm (2.64 eV). Additionally, the photoexcitation of the trapped electrons in V_O defects towards the conduction band may also give absorptions in the visible region. Generally, Ce-MCM-41-type hybrid materials have showed a broad maximum in the UV–vis DRS around 300 nm with a reported band gap of 3.12 eV [16, 33]. The narrowing in the band gap of our synthesized Ce-MCM-41 materials may be associated with defect intermediate energy states present in the band gap of incorporated non-stoichiometric CeO_2 formed with V_O defects and Ce^{3+} ions. Because of the presence of these states, the electrons transition from O 2p to Ce 5d is retarded and, therefore, higher concentration of these defects will further reduced the band gap. As shown in Fig. 5, when photon energy is absorbed from a light source, electrons are transferred from the O 2p valence band to the Ce 4f orbital. Thus, the holes in balance band and the electrons in Ce 4f orbital can generate hydroxyl ($HO^{\cdot}$) and superoxide ($O_2^{\cdot-}$) radicals, respectively. In addition, the holes could transform H_2O and OH^- molecules on the surface of the Ce-MCM-41 hybrid

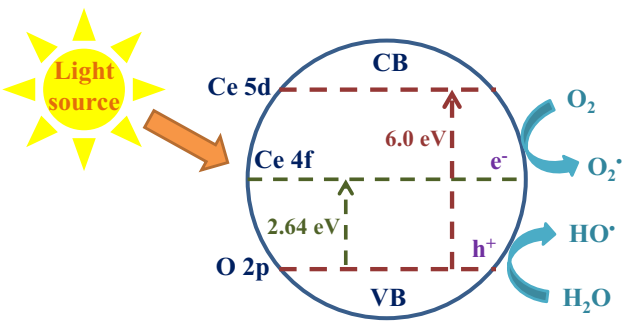

Fig. 5 Schematic representation of different energy level from the incorporated ceria into mesostructured MCM-41 silica composites

materials to form OH radicals, which are highly reactive oxidants that attack the organic compounds adsorbed onto the particle surface to decompose them into mineralized products [34]. Finally, the estimated *Eg* values are consistent taking into account the particle size of the mesoporous ceria-silica composites obtained by the FE-SEM images (Fig. 2a–c). The band gap exhibited in the Ce-MCM-41 materials with low and mid Ce loading (Si/Ce = 50, 30) could be associated with the presence of big nanometric particles of ~ 600 and ~ 500 nm, respectively, compared with those that constitute the mesoporous ceria-silica composite with high Ce content (Si/Ce = 10) which presented nanoparticles with a size of ~ 300 nm. According to estimation method reported by Wouters et al. [35], for these Ce-doped silicates, the concentration of silanols groups is remarkably constant at about 14.1 mmol per gram, irrespective of the Ce loading (Table 1).

3.5 Surface Ce^{4+}/Ce^{3+} distribution and oxygen defects formation—XPS and Raman spectroscopic analysis

XPS analysis is generally used to obtain the information related to oxidation states and relative surface atomic ratios of various samples. Figure 6 shows Ce3d core level XPS spectra of pure CeO_2 and Ce-MCM-41 hybrid materials. It is apparent from this figure that all Ce3d XPS spectra are complex and are formed of several individual overlapping peaks. As clearly shown in Fig. 6a, Ce3d XPS spectrum pertaining to pure CeO_2 is composed of two multiplets, labeled as *u* and *v*, corresponding to the spin–orbit coupling of $3d_{3/2}$ and $3d_{5/2}$ levels, respectively, [17, 36, 37]. The contributions denoted as *u‴* (916.9 eV) and *v‴* (898.3 eV), *u″* (908.4 eV) and *v″* (889.3 eV), *u* (900.8 eV) and *v* (882.6 eV), correspond to Ce^{4+} cations, specifically related with $Ce3d^94f^0O2p^6$, $Ce3d^94f^2O2p^4$ and $Ce3d^94f^1O2p^5$ final states [30]. Additionally, the signals *u′* (904.5 eV) and *v′* (885.1 eV), u_0 (899.2 eV) and v_0 (878.5 eV), are ascribed to photoemission of Ce^{3+} and correspond to a mixture of the $Ce3d^94f^1O2p^6$ and $Ce3d^94f^2O2p^5$ final states [26, 37]. In the spectrum of Fig. 6a, the *u‴* peak is the most convenient feature to identify the progress of cerium reduction, because it does not overlap with others peaks. Meanwhile, the two characteristic valleys of the spectrum, centered between *u″* and *u* peaks (denoted as *u′*) and *v″* and *v* peaks (denoted as *v′*), respectively, can be taken into account for a qualitative estimation of the degree of reduction of Ce^{4+} [25].

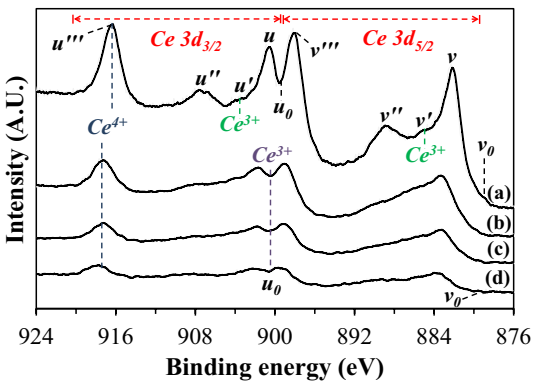

Fig. 6 Ce 3d XPS spectra of the Ce-doped MCM-41 silicas. (*a*) CeO_2, (*b*) Ce-MCM-41-10, (*c*) Ce-MCM-41-30 and (*d*) Ce-MCM-41-50

On the other hand, considering the uncertainty of the instrument used for XPS studies (± 0.2 eV), the displacement slightly observed of ~ 1.0 eV for the doublets in the Ce3d XPS spectra of the Ce-MCM-41 hybrid materials (Fig. 6b–d) may be due to an charge effect caused by the chemical environment. Nonetheless, the peaks *u‴* (917.5 eV) and *v‴* (899.1 eV) originated from $Ce3d^94f^0O2p^6$ final state of Ce^{4+} are still clearly observed. Here, the greatest contribution of Ce^{3+} to the Ce3d spectra was indicated by a doublet pair of u_0 (900.3 eV) and v_0 (879.3 eV) which correspond to $Ce3d^94f^1O2p^6$ final state. In this sense, qualitatively, the peak areas corresponding to the ions must be proportional to their concentration. Thus, if Ce-MCM-41 samples contain only a small amount of Ce^{3+} ions, then the valley u_0 is very well defined. On the contrary, if the reduction degree of $Ce^{4+} \rightarrow Ce^{3+}$ is high, the valley begins to vanish due to an increase in the Ce^{3+} ions concentration. Based on these hypotheses, it can be concluded from Fig. 6b–d that Ce-MCM-41 hybrid materials have a mixture of Ce^{3+}/Ce^{4+} cerium species on their surface, with Ce^{4+} species apparently being predominant. In addition, a closer look at this figure reveals a progressive decrease in the intensities of the *u‴* and *v‴* peaks along with an increase in the intensity of the Ce^{3+}3d photoemission peaks (u_0 and v_0). This observation confirms that there is an increase in the Ce^{3+} ions concentration over surface, and thus more oxygen vacancies (V_O), as result of a lower Ce content incorporated into Ce-MCM-41 hybrid materials.

The Raman spectra shown in Fig. 7 indicated the formation of cubic phase CeO_2 (JCPDS 65-5923) incorporated into silicate framework of mesostructured Ce-MCM-41 hybrid materials. First, in the case of semiconductor CeO_2 nanoparticles, the peak of higher intensity present around 460 cm^{-1} in the spectrum of the Fig. 7A is ascribed to F_{2g} Raman active mode for CeO_2 with a fluorite-type crystalline structure [38]. This F_{2g} signal is attributed to symmetrical stretching mode of Ce-O8 vibrational unit and is assigned to second order transverse acoustic (2TA) mode [39]. Apart from the F_{2g} peak, the Raman spectrum of CeO_2 exhibits three additional lower intensity contributions at 242, 584 and 1173 cm^{-1}, respectively. Weak peak at 242 cm^{-1} is associated with the doubly degenerate transverse optical (2TO) mode and the moderately intense peak at 584 cm^{-1}

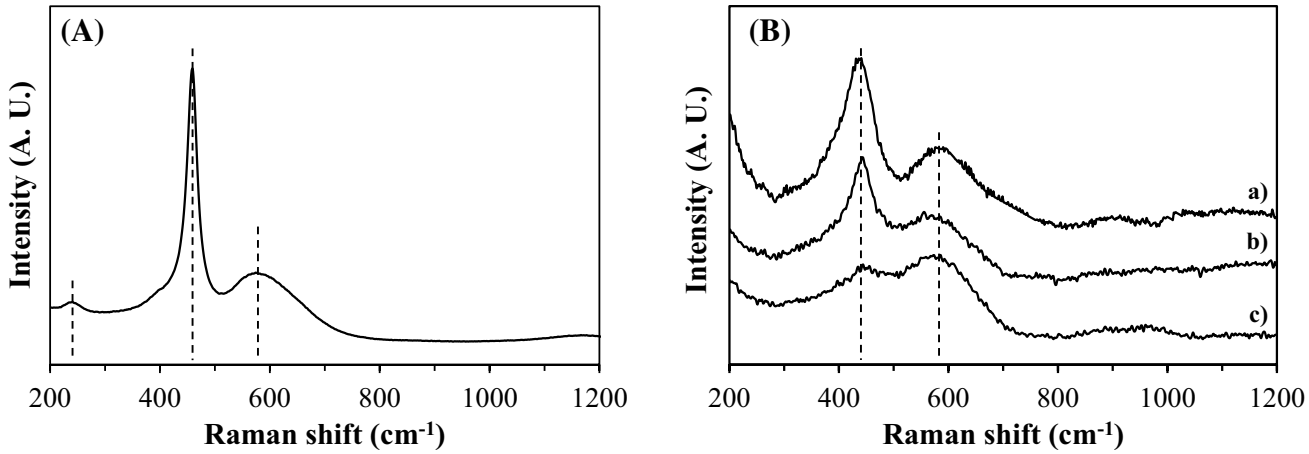

Fig. 7 Raman spectra of (**A**) pure CeO_2 and (**B**) Ce-MCM-41 hybrid materials. (*a*) Ce-MCM-41-10, (*b*) Ce-MCM-41-30 and (*c*) Ce-MCM-41-50

corresponds to non-degenerate longitudinal optical (LO) mode [40]. This LO mode is associated with formation of intrinsic oxygen vacancies (V_O), and therefore with the Ce^{3+} ions, present in ceria lattice [41]. The Raman signal at 1173 cm^{-1} (not clearly identified) is the doubly degenerate longitudinal optical (2LO) mode that is attributed to O–O stretching vibration mode of superoxide anion ($O_2^{\cdot-}$) adsorbed on surface, which is formed by the interaction of the adsorbed oxygen with the electron trapped in the oxygen vacancy [42].

Figure 7B displays the Raman spectra of the Ce-MCM-41 samples. It is observed that the position of F_{2g} signal for these materials is red shifted (442 cm^{-1}) from that position of pure CeO_2. It is speculated that structural defects, such as oxygen vacancies, can interrupt the Ce-O8 vibrational unit, affecting the position of the F_{2g} mode in Ce-MCM-41 materials. In addition, this F_{2g} Raman peak becomes more asymmetric and broadened in the mesostructures than that for pure CeO_2, which might be caused by strain, confinement and the chemical environment present in silicate network. In this sense, the Raman line shape depends on the size distribution of the nanoparticles. If within each Ce-MCM-41 particle the strain is not uniform, the average strain produced by all particles should affect the Raman line position. In our ceria-doped MCM-41 materials, the particle sizes are not uniform, and hence, collective strain coming from all the particles will not be the same. Thus, both the red shift and peak asymmetry are due to this non-uniform strain present in Ce-MCM-41 hybrid materials. Additionally, it can be expected that the fluorite-type crystalline structure of incorporated ceria has suffered a considerable distortion or an expansion of Ce–O–Ce lattice as result of the presence of V_O defects and Ce^{3+} ions [43]. Nonetheless, as can be seen in the Raman spectra, the F_{2g} peak intensity rises depending of the amount of Ce grafted in the silicate framework of the Ce-MCM-41 hybrid materials. On the other hand, the peak at 592 cm^{-1} corresponds to oxygen vacancies originated from nonstoichiometry in the ceria incorporated into MCM-41 mesostructure. The relatively high intensity of this peak in spectra of Fig. 7B indicates that a discreet amount of oxygen vacancies are present in the Ce-MCM-41 nanoparticles. However, this signal confirmed that the incorporation of a low amount of Ce ions into MCM-41 mesostructure (e.g. Si/Ce = 50) can generate more V_O defects in comparison to that Ce-MCM-41 material with high Ce content. Finally, it should be noted that all Raman spectra of the Ce-MCM-41 hybrid materials indicated the formation of a Si–Ce solid solution via their surfactant assisted hydrothermal synthesis.

In order to explain both the formation of V_O defects and the presence of Ce^{3+} ions by the reversible reduction and oxidation processes ($CeO_2 \leftrightarrow CeO_{2-x} + x/2O_2(g)$, $0 \le x \le 0.5$) in the ceria-modified mesoporous MCM-41 solids, the photoexcitation process represented by Kroger-Vink notation (Eq. 1) can be adopted [44].

$$4Ce_{Ce} + O_O \rightarrow 2Ce_{Ce} + 2Ce'_{Ce} + V_{\ddot{O}} + 0.5O_2(g) \quad (1)$$

where Ce_{Ce} and Ce'_{Ce} represent a Ce^{4+} and Ce^{3+} ion in a cerium lattice site, respectively. The O_O symbol serve as O^{2-} ion on oxygen lattice site, and $V_{\ddot{O}}$ is assigned to a neutral oxygen vacancy in the oxygen lattice site. Thus, formation of $V_{\ddot{O}}$ in CeO_2 releases two electrons which are captured by two Ce^{4+} ions and transformed into Ce^{3+} ions. The localization of an electron on a Ce^{4+} ion (ionic radius = 0.1098 nm) converts Ce^{4+} to the slightly larger Ce^{3+} ion (ionic radius = 0.1283 nm) with one electron in the 4f orbital. On the contrary, when a defective phase (CeO_{2-x}) is oxidized, two 4f electrons from the two neighboring Ce^{3+} ion sites move to the site where an oxygen atom is incorporated and then delocalize into the O 2p valence band. Therefore, the reversible processes of oxidation and reduction for ceria

(e.g. $CeO_2 \leftrightarrow CeO_{1.5} + 0.25O_2(g)$) have been considered to involve the extreme states of the Ce 4f electrons in which they are fully delocalized and localized, respectively [45], as discussed above in the XPS analysis. In addition, Skorodumova et al. [45] affirmed that the remarkable macroscopic properties of ceria to store, release and transport oxygen is due to the quantum process of electron localization. In this process the two electrons which remain when oxygen leaves the lattice (V_O defects formation) are localized on two cerium atoms, turning Ce^{4+} to Ce^{3+}. Therefore, if impurities are present in small amounts and segregate to the surface, chemical activity of the surface may be affected.

4 Conclusions

We studied the effect of Ce incorporation into mesoporous MCM-41 silica on its structural and optical properties. Isomorphic substitution of Si^{4+} by Ce^{4+} in the ceria-silica composites via hydrothermal method in static conditions induces formation of Ce^{3+} ($4f^1$) cationic ions and V_O defects on the lattice site and surface. Based on XPS analysis, Ce-MCM-41 hybrid materials have a Ce^{3+}/Ce^{4+} species mixture on their surface, with Ce^{4+} species apparently being predominant. Depending of the grafted Ce quantity, the structural defects concentration extends the absorption edge. For example, the oxygen deficient Ce-MCM-41-50 nanoparticles (600 nm) with low Ce-loading (5.5 wt%) has high specific area (884 m^2/g), narrow band gap (2.64 eV) and big concentration of free electrons and holes on the surface. Only a low degree of Ce-doping in the mesostructured MCM-41 silica leads preferably to an electrons transition from O 2p to Ce 4f orbitals and/or Ce 4f to Ce5d orbitals when photon energy is absorbed from a visible light source. The expansion of lattice and generation of crystal strain confirm that the local structure of ceria in Ce-MCM-41 materials has nonstoichiometric defects as oxygen vacancies. These V_O defects lead to asymmetry and shifting in Raman active peak, and also result in effective red shifting of band gap. Nonetheless, these materials have some advantages over other solids such as: (i) availability of a very high specific area to disperse active phases; (ii) a high efficiency to light absorption; and (iii) a rich surface in hydroxyl groups. These make them promising photocatalysts for different applications as the elimination of organic compounds, wastewater treatment and photochemical CO_2 conversion. Efforts are going on to apply these interesting new observations to eliminate certain contaminants (e.g. methyl orange) from wastewater using visible light.

Acknowledgements O.A. González Vargas thanks the Instituto Politécnico Nacional (IPN), Mexico, for financial aid to carry out this research. We are grateful to Dr. H. Martinez Gutierrez and Dr. Luis Lartundo Rojas (CNMN-IPN, Mexico) for their kind cooperation with FE-SEM, SEM-EDS and XPS experiments. The authors would like to acknowledge the financial support from IPN, Mexico (SIP-20170900).

References

1. C. Aprile, A. Corma, H. Garcia, Phys. Chem. Chem. Phys. **10**, 769–783 (2008)
2. Y. Kuwahara, H. Yamashita, J. Mater. Chem. **21**, 2407–2416 (2011)
3. D.P. Sahoo, D. Rath, B. Nanda, K.M. Parida, RSC Adv. **5**, 83707–83724 (2015)
4. F. Fresno, R. Portela, S. Suaréz, J.M. Coronado, J. Mater. Chem. A **2**, 2863–2884 (2014)
5. S. Suarez, in *Design of Advanced Photocatalytic Materials for Energy and Environmental Applications*, ed. By J.M. Coronado, F. Fresno, M.D. Hernández-Alonso, R. Portela (Springer, London, 2013), p. 171
6. A.D. Liyanage, S.D. Perera, K. Tan, Y. Chabal, K.J. Balkus Jr., ACS Catal. **4**, 577–584 (2014)
7. Z.M. Yang, G.F. Huang, W.Q. Huang, J.M. Wei, X.G. Yan, Y.Y. Liu, C. Jiao, Z. Wan, A. Pan, J. Mater. Chem. A **2**, 1750–1756 (2014)
8. N.S. Arul, D. Mangalaraj, R. Ramachandran, A.N. Grace, J.I. Han, J. Mater. Chem. A **3**, 15248–15258 (2015)
9. M.J. Islam, D.A. Reddy, J. Choi, T.K. Kim, RSC Adv. **6**, 19341–19350 (2016)
10. D. Yin, F. Zhao, L. Zhang, X. Zhang, Y. Liu, T. Zhang, C. Wu, D. Chen, Z. Chen, RSC Adv. **6**, 103795–103802 (2016)
11. X. Liu, K. Zhou, L. Wang, B. Wang, Y. Li, J. Am. Chem. Soc. **131**, 3140–3141 (2009)
12. Y. Kang, M. Sun, A. Li, Catal. Lett. **142**, 1498–1504 (2012)
13. O.A. González Vargas, J.A. de los Reyes Heredia, A. Montesinos Castellanos, L.F. Chen, J.A. Wang, Mater. Chem. Phys. **139**, 125–133 (2013)
14. A. Sayary, Y. Yang, M. Kruk, M. Jaroniec, J. Phys. Chem. B **103**, 3651–3658 (1999)
15. S.B. Hartono, S.Z. Qiao, J. Liu, K. Jack, B.P. Ladewig, Z. Hao, G.Q.M. Lu, J. Phys. Chem. C **114**, 8353–8362 (2010)
16. N. Pal, E.-B. Cho, D. Kim, RSC Adv. **4**, 9213–9222 (2014)
17. L. Katta, P. Sudarsanam, B. Mallesham, B.M. Reddy, Catal. Sci. Technol. **2**, 995–1004 (2012)
18. Q. Huo, D.I. Margolese, G.D. Stucky, Chem. Mater. **8**, 1147–1160 (1996)
19. O.A. González Vargas, J.A. de los Reyes Heredia, J.A. Wang, L.F. Chen, A. Montesinos Castellanos, M.E. Llanos, Int. J. Hydrogen Energy **38**, 13914–13925 (2013)
20. N. Pal, E.-B. Cho, D. Kim, C. Gunathilake, M. Jaroniec, Chem. Eng. J. **262**, 1116–1125 (2015)
21. E.-B. Cho, S. Yim, D. Kim, M. Jaroniec, J. Mater. Chem. A **1**, 12595–12605 (2013)
22. F. Goubin, X. Rocquefelte, M.H. Whangbo, Y. Montardi, R. Brec, S. Jobic, Chem. Mater. **16**, 662–669 (2004)
23. A. Bensalem, J.C. Muller, F. Bonzon-Verduraz, J. Chem. Soc. Faraday Trans. **88**, 153–154 (1992)
24. S. Shi, X. Ke, C. Ouyang, H. Zhang, H. Ding, Y. Tang, W. Zhou, P. Li, M. Lei, W. Tang, J. Power Sources **194**, 830–834 (2009)
25. P. Ji, J. Zhang, F. Chen, M. Anpo, J. Phys. Chem. C **112**, 17809–17813 (2008)
26. N.K. Renuka, A.K. Praveen, C.U. Aniz, Microporous Mesoporous Mater. **169**, 35–41 (2013)
27. S. Phoka, P. Laokul, E. Swatsitang, V. Promarak, S. Seraphin, S. Maensiri, Mater. Chem. Phys. **115**, 423–428 (2009)

28. P. Patsalas, S. Logothetidis, L. Sygellou, S. Kennou, Phys. Rev. B **68**, 035104 (2003)
29. B. Tatar, E.D. Sam, K. Kutlu, M. Ürgen, J. Mater. Sci. **43**, 5102–5108 (2008)
30. Y. Wang, J. Zhao, T. Wang, Y. Li, X. Li, J. Yin, C. Wang, J. Catal. **337**, 293–302 (2016)
31. P.J. Hay, R.L. Martin, J. Uddin, G.E. Scuseria, J. Chem. Phys. **125**, 34712 (2006)
32. L. Jiang, M. Yao, B. Liu, Q. Li, R. Liu, H. Lu, J. Phys. Chem. C **116**, 11741–11745 (2012)
33. S.C. Laha, P. Mukherjee, S.R. Sainkar, R. Kumar, J. Catal. **207**, 213–223 (2002)
34. B. Choudhury, P. Chetri, A. Choudhury, RSC Adv. **4**, 4663–4671 (2014)
35. B.H. Wouters, T. Chen, M. Dewilde, P.J. Grobet, Microporous Mesoporous Mater. **44–45**, 453–457 (2001)
36. M.J. Muñoz-Batista, M.N. Gómez-Cerezo, A. Kubacka, D. Tudela, M. Fernández-Garcia, ACS Catal. **4**, 63–72 (2014)
37. S. Luo, T.D. Nguyen-Phan, A.C. Johnston-Peck, L. Barrio, S. Sallis, D.A. Arena, S. Kundu, W. Xu, L.F.J. Piper, E.A. Stach, D.E. Polyanskiy, E. Fujita, J.A. Rodriguez, S.D. Senanayake, J. Phys. Chem. C **19**, 2669–2679 (2015)
38. T. Suzuki, I. Kosacki, H.U. Anderson, P. Colomban, J. Am. Ceram. Soc. **84**, 2007–2014 (2001)
39. I. Kosacki, T. Suzuki, H.U. Anderson, P. Colomban, Solid State Ion. **149**, 99–105 (2002)
40. B. Choudhury, A. Choudhury, Mater. Chem. Phys. **131**, 666–671 (2012)
41. Z.V. Popović, Z. Dohčević-Mitrović, M.J. Konstantinović, M. Šćepanović, J. Raman Spectrosc. **38**, 750–755 (2007)
42. S. Aškravić, Z. Dohčević-Mitrović, A. Kramenović, N. Lazarević, V. Kahlenberg, Z.V. Popović, J. Raman Spectrosc. **43**, 76–81 (2012)
43. L. Wu, H.J. Wiesmann, A.R. Moodenbaugh, R.F. Klie, Y. Zhu, D.O. Welch, M. Suenaga, Phys. Rev. B: Condens. Matter Mater. Phys. **69**, 125415 (2004)
44. E. Shoko, M.F. Smith, R.H. McKenzie, J. Phys.: Condens. Matter. **22**, 223201 (2010)
45. N.V. Skorodumova, S.I. Simak, B.I. Lundqvist, I.A. Abrikosov, B. Johansson, Phys. Rev. Lett. **89**, 166601 (2002)